The Astrophysical Journal, 923:180 (15pp), 2021 December 20 https://doi.org/10.3847/1538-4357/ac2f9c

Skew-kappa Distribution Functions and Whistler Heat Flux Instability in the Solar Wind: The Core-strahlo Model

Bea Zenteno-Quinteros[1], Adolfo F. Viñas[2,3], and Pablo S. Moya[1]
[1] Departamento de Física, Facultad de Ciencias, Universidad de Chile, Santiago, Chile; beatriz.zenteno@ug.uchile.cl, pablo.moya@uchile.cl
[2] Department of Physics & the Institute for Astrophysics and Computational Sciences (IACS), Catholic University of America, Washington, DC, 20064, USA
[3] NASA Goddard Space Flight Center, Heliospheric Science Division, Geospace Physics Laboratory, Mail Code 673, Greenbelt, MD 20771, USA
Received 2021 January 29; revised 2021 October 12; accepted 2021 October 12; published 2021 December 21

Abstract

Electron velocity distributions in the solar wind are known to have field-aligned skewness, which has been characterized by the presence of secondary populations such as the halo and strahl. Skewness may provide energy for the excitation of electromagnetic instabilities, such as the whistler heat flux instability (WHFI), which may play an important role in regulating the electron heat flux in the solar wind. Here we use kinetic theory to analyze the stability of the WHFI in a solar-wind-like plasma where solar wind core, halo, and strahl electrons are described as a superposition of two distributions: a Maxwellian core, and another population modeled by a Kappa distribution to which an asymmetry term has been added, representing the halo and also the strahl. Considering distributions with small skewness, we solve the dispersion relation for the parallel-propagating whistler mode and study its linear stability for different plasma parameters. Our results show that the WHFI can develop in this system and provide stability thresholds for this instability, as a function of the electron beta and the parallel electron heat flux, to be compared with observational data. However, since different plasma states, with different stability level to the WHFI, can have the same moment heat flux value, it is the skewness (i.e., the asymmetry of the distribution along the magnetic field), and not the heat flux, that is the best indicator of instabilities. Thus, systems with high heat flux can be stable enough to WHFI, so that it is not clear whether the instability can effectively regulate the heat flux values through wave–particle interactions.

Unified Astronomy Thesaurus concepts: Solar wind (1534); Space plasmas (1544)

1. Introduction

Space plasmas are magnetized systems that can be out of thermal equilibrium owing to the low collision frequency between their constituent particles. Coulomb collisions are an efficient mechanism to relax particle populations to thermodynamic equilibrium, where the distribution functions reduce to Maxwellian profiles. Therefore, on collisionless systems the particles' velocity distribution function can develop nonthermal features. These nonthermal characteristics represent free energy in the system, which can be emitted as electromagnetic radiation, such that the plasma relaxes to more stable states via noncollisional processes as wave–particle interactions.

The solar wind shows several nonthermal features in the electron velocity distribution (eVDF). Among them, the field-aligned skewness (Feldman et al. 1975; Scudder & Olbert 1979; Marsch et al. 1982, 2004; Pilipp et al. 1987; Salem et al. 2003; Nieves-Chinchilla & Viñas 2008) is clearly observed. This asymmetry provides the energy to excite different modes, depending on the plasma parameters (Gary et al. 1975; Shaaban et al. 2018a). One of these modes corresponds to the so-called whistler heat flux instability (WHFI), and the excitation of this branch is due to the free energy provided by the skewness or asymmetry of the eVDF. The WHFI has received attention throughout the years because the associated whistler waves are one of the main candidates for a noncollisional regulation of the electron heat flux values in the solar wind (Abraham-Shrauner & Feldman 1977a; Gary et al. 1994; Scime et al. 1994, 2001; Gary & Li 2000; Lacombe et al. 2014; Kuzichev et al. 2019; Shaaban et al. 2019b).

There is ample observational evidence that the electron heat flux in the solar wind cannot be fully described by the collisional Spitzer–Harm theory (Spitzer & Härm 1953). This model is able to adequately describe measurements of the heat flux under slow solar wind conditions, but in many other cases the Spitzer–Harm law predicts higher values than those shown by in situ measurements at 1 au from the Sun (Bale et al. 2013). This phenomenon of depletion of the electron heat flux below the values predicted by the collisional transport model has been studied for decades. For example, empirical calculations have been carried out in order to reproduce the measured heat flux values through an ad hoc reduction of the thermal conductivity (Cuperman et al. 1972). Theoretical models have also been proposed, considering different physical mechanisms that can potentially regulate the electron heat flux through collisionless mechanisms (Forslund 1970; Hollweg & Jokipii 1972; Landi et al. 2012). The most accepted mechanism to explain this suppression corresponds to a noncollisional regulation due to the kinetic process of wave–particle interaction (Perkins 1973; Hollweg 1974; Scime et al. 1994). The main candidate for constraining the electron heat flux values are the whistler waves excited by the heat flux instability; however, the dominant wave mode involved in this noncollisional regulation process is still under debate (Gary & Feldman 1977; Scime et al. 2001; Bale et al. 2013; Shaaban et al. 2018b; López et al. 2020a).

Most studies of the solar wind electron skewness assumed that the electron populations are composed of different subpopulations, each modeled by a Maxwellian, bi-Maxwellian, or Kappa

distribution, which combined can form a skew nonthermal distribution. An example of this in the solar wind is the linear superposition of the drifting electron core, halo, and strahl populations (Štverák et al. 2009; Saeed et al. 2016; Lazar et al. 2018; López et al. 2020a). Note that these typical distribution functions are symmetrical by themselves and do not show any skewness. Under this context, in recent years studies have been developed where less common functions are used to model the electron subpopulations. The particularity of these "new" ad hoc functions is that they are, in fact, asymmetrical. For example, in Horaites et al. (2018a) the authors analyze the kinetic stability of a plasma where the strahl population is described by an analytic function, which was derived from the collisional kinetic equation. Also, in Vasko et al. (2019) the authors modeled the strahl population by means of a bi-Maxwellian function to which extra parameters were added, which allows the modification of its symmetry.

Along the same line, here we propose a new heuristic model for solar wind electrons that can reproduce the behavior of a core-halo-strahl representation but using only two subpopulations: a bi-Maxwellian core plus a modification to the Kappa distribution that introduces skewness, representing the halo and strahl electrons in a single skew distribution. This skew-Kappa distribution was first proposed by Beck (2000) in a study of fluid turbulence. In the original derivation, the author showed that the asymmetry of the VDF is related to the level of turbulence of the media, measured by the Reynolds number. The aim of this work is to study, using kinetic linear theory, the effect of nonthermal electrons described by a skew-kappa-like function on the excitation of parallel-propagating whistler modes associated with the WHFI in a noncollisional, magnetized, solar-wind-like plasma. We will show that the proposed eVDF reproduces the main field-aligned features of the eVDF as observed in the solar wind, potentially allowing simpler models of solar wind electrons modeled as a superposition of two subpopulations. In addition, considering a unified description of halo and strahl electrons may also be relevant for the understanding of the relevance of the electron nonthermal features for the dynamics of the heat transport by the solar wind (Bale et al. 2013), as well as the kinetic physics governing the halo formation and its relation to the strahl (Vocks et al. 2005; Horaites et al. 2017, 2018b).

The paper is organized as follows: In Section 2 we present our model, analyze the skew-kappa-like function, and introduce it as a new distribution function for describing the halo and strahl electron populations. In Section 3 we show the theoretical results of linear kinetic theory for the dispersion tensor of parallel-propagating waves, in a plasma where the electron population is modeled by a core and skew-kappa-like function. Then, in Section 4 we systematize this analysis in order to obtain the marginal stability thresholds for this distribution as a function of plasma beta and heat flux, and we present the best-fit parameters for these contours. Finally, in Section 5 we summarize and discuss our results.

2. Electron Distribution: The Core-strahlo Model

We model the solar wind electrons distribution function f_e as a superposition of two subpopulations:

$$f_e(v_\perp, v_\parallel) = f_c(v_\perp, v_\parallel) + f_s(v_\perp, v_\parallel). \quad (1)$$

The first is a bi-Maxwellian distribution (f_c) representing the core

$$f_c(v_\perp, v_\parallel) = \frac{n_c}{\pi^{3/2}\alpha_\perp^2\alpha_\parallel}\exp\left(-\frac{v_\perp^2}{\alpha_\perp^2} - \frac{(v_\parallel - U_c)^2}{\alpha_\parallel^2}\right), \quad (2)$$

and the second is a skew-Kappa function (f_s) to describe both the halo and strahl electrons, which from now on we will call the "strahlo," and this representation of solar wind electrons we will call "the core-strahlo model." Under this model f_s consists of a Kappa function to which an asymmetry term has been added, namely,

$$f_s(v_\perp, v_\parallel) = n_s A_s\left[1 + \frac{1}{\kappa_s - \frac{3}{2}} \times \left(\frac{v_\perp^2}{\theta_\perp^2} + \frac{v_\parallel^2}{\theta_\parallel^2} + \delta_s\left(\frac{v_\parallel}{\theta_\parallel} - \frac{v_\parallel^3}{3\theta_\parallel^3}\right)\right)\right]^{-(\kappa_s+1)}. \quad (3)$$

In both distribution functions, the subscripts $\parallel$ and $\perp$ are with respect to the background magnetic field, and n_c and n_s denote the number density of the core and strahlo, respectively. In Equation (2) $\alpha_\perp$ and $\alpha_\parallel$ are the thermal speeds, and U_c is the drift of the core. Also, in Equation (3) A_s is a normalization term such that $\iint f_s\, d\boldsymbol{v} = n_s$, and $\theta_\parallel$ and $\theta_\perp$ are related to the thermal velocities as defined in Equations (A8) and (A6), respectively. Also, κ_s is a measurement of the deviation of this function from a Maxwellian distribution, and δ_s controls the field-aligned skewness. Note that when $\delta_s = 0$ we recover the well-known Kappa distribution (Olbert 1968; Vasyliunas 1968; Scudder 1996; Maksimovic et al. 2005; Xiao et al. 2006; Lazar et al. 2016, 2017; Viñas et al. 2017).

2.1. Validity of the Model

Depending on the value of the κ_s and δ_s parameters, Equation (3) may become negative, complex, or multivalued, which imposes some caveats and limitations on the use of the skew-Kappa for the eVDF. In particular, for an arbitrary value of δ_s and κ_s there is a particular value $u = v_\parallel/\theta_\parallel$ in which the skew-Kappa distribution diverges following a vertical asymptote. This value corresponds to the real solution of the following equation:

$$\kappa_s - \frac{3}{2} + \frac{v_\parallel^2}{\theta_\parallel^2} + \delta_s\left(\frac{v_\parallel}{\theta_\parallel} - \frac{v_\parallel^3}{3\theta_\parallel^3}\right) = 0, \quad (4)$$

which always exists for real values of κ_s and δ_s. The dependency of u is strong and weak with respect to δ_s and κ_s, respectively. For example, for $\delta_s = 0.1$, the real solutions of Equation (4) are $u \simeq 30.1$ for $\kappa_s = 3$ and $u \simeq 30.4$ for $\kappa_s = 10$. Furthermore, in the case of $\delta_s = 0.2$, the values are $u \simeq 15.3$ and $u \simeq 15.7$ (in units of the thermal speed of the strahlo) for $\kappa_s = 3$ and $\kappa_s = 10$, respectively. Moreover, due to the peak of the VDF at $\boldsymbol{v} \simeq 0$ and the presence of the mentioned asymptote, the distribution always has a local minima at $u_{\min}$, with $0 < u_{\min} < u$, given by the solution of the derivative of

Equation (4), namely,

$$u_{\min} = \frac{v_{\parallel \min}}{\theta_{\parallel}} = \frac{1 + \sqrt{1 + \delta_s^2}}{\delta_s}, \quad (5)$$

a monotonically decreasing function of δ_s, with $u_{\min} \simeq 20.0$ for $\delta_s = 0.1$ and $u_{\min} \simeq 10.1$ for $\delta_s = 0.2$. Therefore, for an arbitrary value of δ_s there is a speed regime in which the integrals necessary to build the moments of the VDF or the dispersion relation will present vertical asymptotes, branch cuts, and poles so that the analytical continuation of the functions in the complex plane may become a quite complicated task. Even though we believe that it may be possible to obtain a bounded reasonable solution, such a calculation for any arbitrary parameters is beyond the scope of this article. Therefore, our skew-kappa model requires careful treatment when selecting the δ_s values.

To avoid these issues, here we apply the heuristic core-strahlo model to situations in which the VDF has small skewness, and the asymptote is far away from the main core in units of the thermal speed, so that we can expand all relevant integrals in a finite Taylor series around $\delta_s = 0$. It is important to mention that since f_s has a vertical asymptote at u, such a Taylor series is not mathematically possible near $v_{\parallel} = u\theta_{\parallel}$. For it to be allowable, the first derivatives of f_s with respect to $\boldsymbol{v}$ must exist, which does not apply for those velocity values that are solutions of Equation (4). However, this mathematical problem can be evaded if all relevant features of the distribution are contained at velocities within the $|v_{\parallel}|/\theta_{\parallel} < |u_{\min}|$ range, i.e., the asymptote of the VDF is far away from the main core. In this case, even though the Taylor series approximation will not be able to mathematically reproduce the exact VDF for all velocity values, calculations based on the approximated version of the VDF in the whole velocity domain will allow analytic calculations, keeping all of the relevant physical properties of the skew-Kappa distribution, which subsequently will lead to a direct interpretation of the results and the relevance of each parameter. On the other hand, the general case with arbitrary skewness, when the asymptote may be closer to the main core of the VDF, remains to be solved. In such a case the Taylor expansion approach may not be an adequate representation of the VDF near the singularity, and other functional expressions with more attractive properties in the complex plane could be a better option. Under this context, another way to approximate the initial distribution for arbitrary skewness may be the expansion of Equation (3) on a different base. After a preliminary analysis, it seems that the Padé approximant (Bender & Orszag 1999) may be a reasonable procedure for such an endeavor, as this approximation does not present new singularities. We will leave this analysis to a future study. From now on we will consider small values of δ_s, such that $\delta_s^3 \ll 1$, and we will make use of a Taylor expansion of Equation (3) up to order δ_s^2 (see Equation(A1) in Appendix A).

Figure 1 shows parallel cuts at $v_{\perp} = 0$ of the eVDF considering isotropic subpopulations with $n_s/n_e = 0.1$, $T_{\parallel s}/T_{\parallel c} = 7.0$, and different choices of κ_s and δ_s. Top and bottom panels show the skew-Kappa strahlo (given by Equation (3) and the total eVDF (Equation (1)), respectively, comparing the exact distribution with a Taylor expansion of up to order δ_s^2 as shown in Equation (A1) in Appendix A. In addition, vertical dotted lines indicate the value of $v_{\min}$ given by Equation (5). From the figure we can see that within the $|v_{\parallel}| < |v_{\min}|$ velocity range the exact and approximated versions of the VDF are mostly the same. In particular, all relevant features of the VDF, such as the skewness and suprathermal tails, can be clearly observed in both representations inside the $|v_{\parallel}| < |v_{\min}|$ velocity range (as we will see in Section 2.2). Thus, as all physical properties of the VDF are covered (shape, moments, and dispersion properties) in the small skewness regime ($\delta_s^3 \ll 1$), a second-order approximation of electrons following a skew-Kappa distribution given by Equation (3) can be reasonably represented by the Taylor expansion as shown in Equation (A1). In this case all the dispersion functions are reduced to a superposition of standard integrals of the Kappa distribution in $v_{\parallel}$ similar to the Q integral given by Equation (5) in Mace & Hellberg (1995) or Equation (12) in Hellberg & Mace (2002), a regime already well investigated for integer (Summers & Thorne 1991) or arbitrary (Mace & Hellberg 1995; Hellberg & Mace 2002) values of the κ_s parameter.

To further ascertain the validity of the expansion and the dispersion relation analysis results for the heat flux instability, we have carried out a comparison of the dispersion properties between a core-halo model based on drifting Maxwellian distributions and those of the skew-Kappa core-strahlo model, using the same parameters (see Figures 4(b) and (c) and their discussion in the next section). The dispersion results (shown in Figures 4(b) and (c)) demonstrate that both models essentially reproduce each other quite well. The real frequencies and growth profiles generated by both models are essentially the same.

Finally, it is worth mentioning that since the Kappa functions behave as a power law for large values of the velocity, depending on the value of the κ_s parameter, the moments of the distribution may be divergent, which imposes restrictions for κ_s. In the case of a standard Kappa VDF the pressure is well defined only for $\kappa_s > 3/2$. In our case, to have real and finite values of the temperature and heat flux moments, the values of kappa are restricted to $\kappa_s > 5/2$ (see Appendix A for details). In summary, considering $\delta_s^3 \ll 1$ as in the case of this study, up to second order in δ_s the eVDF is real and positive for all real values of $v_{\parallel}$, and the integrals in the velocity space share the same poles and branch cuts of Kappa distributions (Mace & Hellberg 1995; Hellberg & Mace 2002). Consequently, all the moments of the eVDF and also the dielectric tensor of the plasma are well defined within such caveats.

2.2. Properties of the Core-strahlo Model in the Small Skewness Approximation

Even though the core-strahlo model has several free parameters, quasi-neutrality and zero-current conditions in the ion frame set some relationships between them. In particular, if the ions' density is given by n_p, to ensure quasi-neutrality, we have $n_e = n_c + n_s = n_p$. In other words,

$$\frac{n_c}{n_e} + \frac{n_s}{n_e} = 1. \quad (6)$$

Also, due to the particular shape of the skew-Kappa distribution, for $\delta_s \neq 0$ f_s always has a field-aligned drift $U_s = -\delta_s\theta_{\parallel}/4$. Thus, the zero-current condition imposes the value of U_c to satisfy

$$U_c = \frac{n_s}{n_c}\frac{\delta_s}{4}\theta_{\parallel}. \quad (7)$$

Therefore, under this description, in the ion frame there will be a relative drift $\Delta U_{\parallel}$ between core and strahlo populations given by $\Delta U_{\parallel} = \delta_s\,\theta_{\parallel}(n_e/n_c)/4$. Note that this relative drift is purely due to the skewness of the strahlo. When the electron distribution has no skewness ($\delta_s = 0$), f_e reduces to a symmetrical distribution

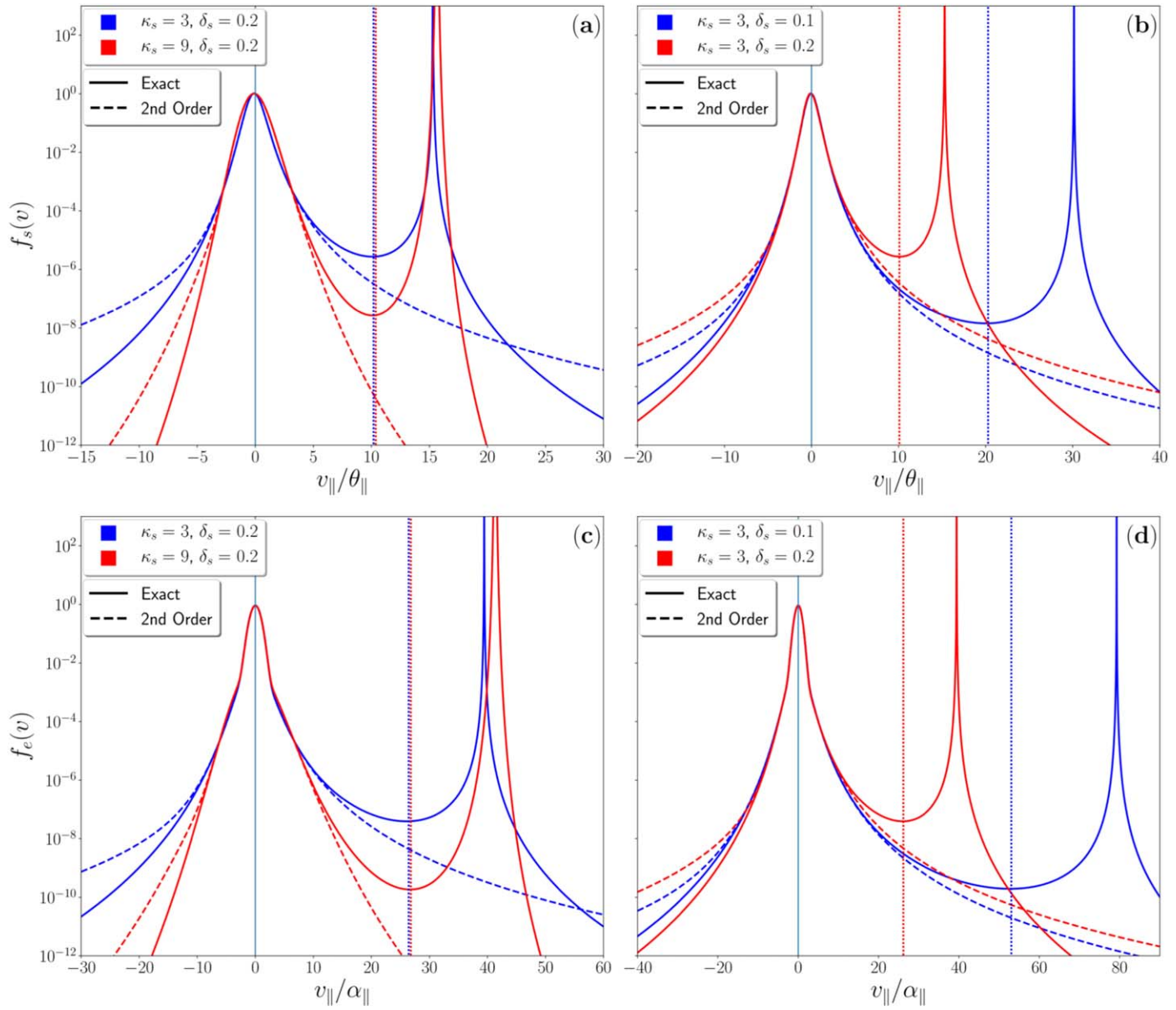

Figure 1. Parallel cuts at $v_\perp = 0$ of the eVDF considering isotropic subpopulations with $n_s/n_e = 0.1$, $T_{\parallel s}/T_{\parallel c} = 7.0$, and different choices of κ_s and δ_s. Top and bottom panels show the skew-Kappa strahlo and the total eVDF, respectively. In each panel solid and dashed lines correspond to the exact VDF and a Taylor expansion up to second order in δ_s, respectively. In addition, vertical dotted lines indicate the local minima of the VDF ($v_{\min}$) given by Equation (5), and velocities are expressed in units of the thermal speed of the strahlo (top) or core (bottom).

with a quasi-thermal core and a nonthermal halo represented by a Kappa distribution (see, e.g., Pierrard et al. 2001; Nieves-Chinchilla & Viñas 2008). For more details, full expressions for the macroscopic parameters and the normalization constant of the strahlo distribution function can be found in Appendix A. It is important to recall that these neutrality and quasi-neutrality conditions are restricted to small skewness values. However, as we will show in Figures 2 and 3, our approximation is able to describe thermal and nonthermal electrons in the solar wind, and the parallel cuts of the eVDF have remarkably similar shapes as previously reported using ISEE-1 (see, e.g., Figure 1(b) in Scudder & Olbert 1979) or Wind (see, e.g., Figure 6 in Nieves-Chinchilla & Viñas 2008) data.

To our knowledge, Beck (2000) was the first to propose this type of skew distributions in a study of fully developed hydrodynamic turbulent flows of skew flow velocity distributions via nonextensive statistical mechanics. Under this context, the author showed that the asymmetry term, which we have denoted as δ_s, is proportional to $\mathrm{Re}^{-1/2}$, where Re is the Reynolds number of the media. This model has been successfully applied to fit data from a turbulent jet experiment (Beck 2000) and environmental atmospheric turbulence (Rizzo & Rapisarda 2004). Here it is worth mentioning that in both cases the adjusted velocity data lie between ± 10 thermal speeds, as shown in Figure 2 of both studies, and that the obtained skewness parameters are small. In addition, the intrinsic mathematical issues of the skew-Kappa distribution discussed in Section 2.1 can be neglected. Therefore, for both cases the skew-Kappa model represents a useful tool to study the relevance and nature of skew velocity distributions in turbulent flows.

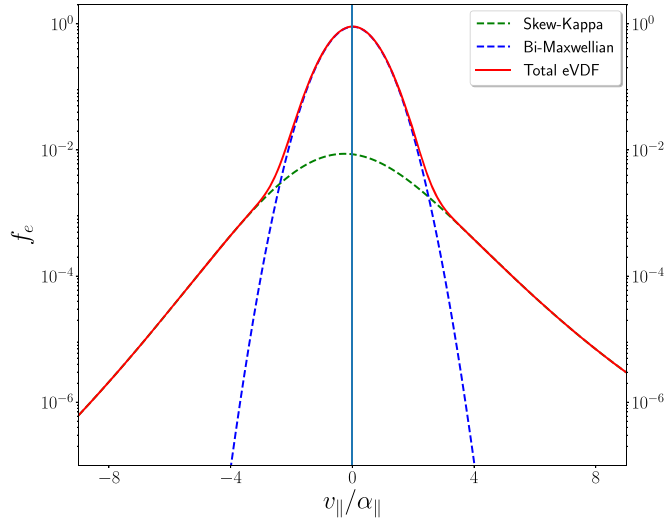

Figure 2. Parallel cuts at $v_\perp = 0$ of the eVDF considering isotropic subpopulations with $n_s/n_e = 0.1$, $T_{\parallel s}/T_{\parallel c} = 7.0$, $\kappa_s = 5$, and $\delta_s = 0.2$. Blue, green, and red curves correspond to core, strahlo, and total eVDF, respectively, and velocity is expressed in units of the thermal speed of the core.

As turbulence is also present in plasma systems, this suggests that these distributions can be more than an ad hoc function for the solar wind electrons. The δ_s parameter can potentially be related to microscopic physical processes that allow the particles to exhibit skew distributions. We strongly believe that this point of view should be further examined and more rigorous theoretical works studying the underlying physics that allows particle distributions to present this nonthermal feature in plasma systems should be developed. However, such a first-principle description is beyond the objective of this paper. Here we focus on accepting and using heuristically this skew-Kappa distribution to describe the skewness and high-energy tails of the eVDF within the aforementioned caveats. This choice allows us to model the eVDF with less free parameters, as an alternative to the usual "core-halo-strahl" models (Štverák et al. 2009; Sarfraz et al. 2016; López et al. 2019; Shaaban et al. 2019a), but at the same time allows us to mimic and study the effect of asymmetry and non-Maxwellian features of the electron population in a solar-wind-like plasma, as well as study their effects on the WHFI excitation.

Figure 2 presents 1D plots at $v_\perp = 0$ of the distribution given by Equation (1) and its two components f_c and f_s as a function of the velocity parallel to the mean magnetic field, in units of the parallel thermal speed of the core. In the figure, blue and green curves represent core and strahlo populations, respectively, and the red curve is the total eVDF. To obtain all of these curves, we fixed the density of the nonthermal population (strahlo) to 10% ($n_s/n_e = 0.1$) and use $T_{\parallel s}/T_{\parallel c} = 7.0$, both of which are solar-wind-like values (Maksimovic et al. 2005; Pierrard et al. 2016; Lazar et al. 2020). We also considered $\delta_s = 0.2$ and $\kappa_s = 5$ and isotropic subpopulations, i.e., $T_{\perp s}/T_{\parallel s} = T_{\perp c}/T_{\parallel c} = 1.0$. The terms $T_{\perp j}$ and $T_{\parallel j}$ correspond to the perpendicular and parallel temperature of population j with respect to the background magnetic field. For the figure we can clearly see that the electron distribution (3) is asymmetric with respect to $v_\parallel = 0$ and that this model maintains typical characteristics of solar wind electrons: a Kappa function with enhanced tails and a narrower Maxwellian core for lower energies. Additionally, we can also see that a positive value of the skewness parameter ($\delta_s > 0$) enhances the skew-Kappa and the total eVDF to the right such that the total skewness of the distribution is positive (along the field lines).

Further, Figure 3 shows 1D plots at $v_\perp = 0$ (left) and contour plots (right) of total distribution (1) for different values of parameters δ_s (top) and κ_s (bottom). In Figures 3(a) and (b) we show how the distribution changes for three different values of the δ_s parameter and a fixed value of $\kappa_s = 5.0$. It is clear in both plots that the strahlo loses its symmetry compared to a Kappa function ($\delta_s = 0$ case), a feature that is more evident in the outermost contours. Also, we can see that for higher δ_s values the more skewed is the distribution. In Figures 3(c) and (d) we show how the distribution changes for three different values of κ_s and fixed $\delta_s = 0.15$. In panel (c) we see that when we increase κ_s, the high-energy tails diminish. This feature is inherited from Kappa distributions, which are reduced to Maxwellian functions in the limit $\kappa \to \infty$. However, unlike Kappas, skew-Kappa distributions never reduced to Maxwellian distributions because they maintain the skewness for all kappa values when $\delta_s \neq 0$. In Figure 3(d) we see that the outer contour seems to shrink proportionally as κ_s decreases while the core does not change, so that the overall contours' shape appears to remain the same. Therefore, this feature suggests that κ_s does not alter the distribution symmetry.

In summary, the combination of Maxwellian and skew-Kappa distributions can model three important nonthermal features observed in the eVDF in the solar wind, namely, quasi-thermal core, enhanced tails, and skewness. Therefore, its use may allow simpler solar wind models, where electrons are modeled as the superposition of core and strahlo, where the distribution skewness is controlled by only one parameter. This field-aligned skewness provides the energy for the excitation of the WHFI, on which we focus the analysis in this work.

3. Linear Theory and Dispersion Relation

We use linear kinetic theory to derive the dispersion relation of wave modes that can propagate in a magnetized, noncollisional, and initially uniform plasma. We perform this calculation in order to analyze the stability of the whistler mode associated with WHFI in a solar-wind-like plasma, where the core-strahlo model is used to describe the electron population. To obtain the dispersion relation, we linearize the Vlasov–Maxwell system of equations. This is a well-known method (Stix 1962; Krall & Trivelpiece 1973) and assumes that the small-amplitude perturbations of the relevant quantities are plane waves, allowing the Vlasov–Maxwell system to be rewritten in the form

$$\mathcal{D}(\omega, \boldsymbol{k}, f_j) \cdot \boldsymbol{E_k} = 0, \tag{8}$$

where $\boldsymbol{E_k}$ is the complex amplitude of the electric field perturbation and $\mathcal{D}(\omega, \boldsymbol{k}, f_j)$ is the dispersion tensor (which is associated with the dielectric tensor of the plasma). This tensor depends on the wavevector $\boldsymbol{k}$, the complex wave frequency $\omega = \omega_r + i\gamma$, and the background distribution functions of the j species composing the plasma f_j. The dispersion relation $\omega = \omega(\boldsymbol{k})$ is determined by the condition $|\mathcal{D}(\omega, \boldsymbol{k}, f_j)| = 0$, so that Equation (8) has nontrivial solutions for $\boldsymbol{E_k}$.

As a first approximation to the problem, we focus our attention on wave modes that propagate parallel to the background magnetic field $\boldsymbol{B_0} = B_0\hat{z}$, so that $\boldsymbol{k} = k\hat{z}$. We make this restriction because the mathematical analysis is greatly simplified compared to the oblique case and because previous works

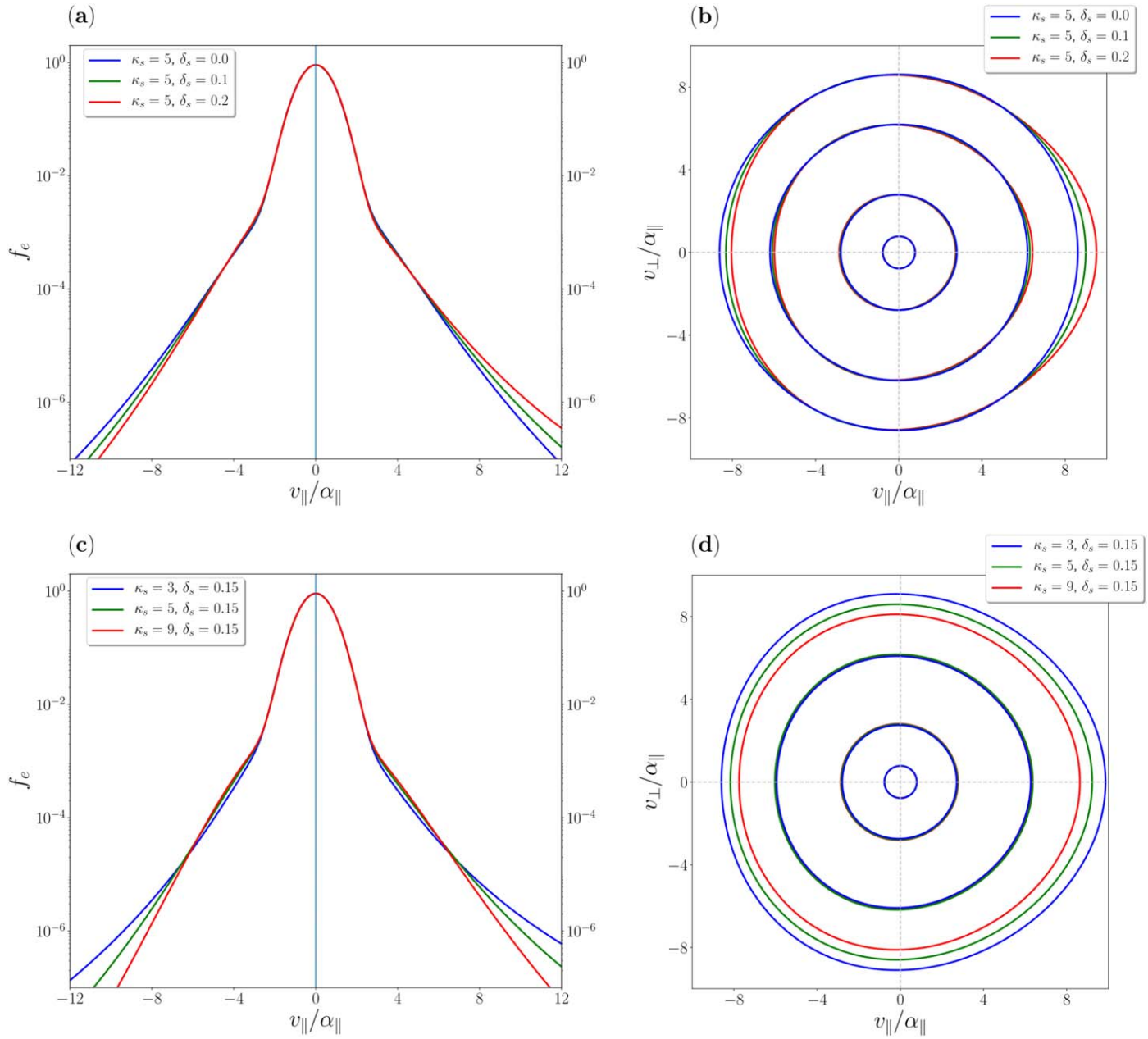

Figure 3. Parallel cuts (left) and contour plots (right) of the eVDF from Equation (1). Top panels consider fixed $\kappa = 5$ and different values of the skewness parameter $\delta_s = 0$ (blue), $\delta_s = 0.1$ (green), and $\delta_s = 0.2$ (red); bottom panels consider fixed skewness ($\delta_s = 0.15$) and different kappa values $\kappa = 3$ (blue), $\kappa = 5$ (green), and $\kappa = 9$ (red). All other parameters are the same as in Figure 2. In panels (b) and (d), from innermost to outermost, the levels plotted correspond to $f(v) = 5 \times 10^{-1}$, 2×10^{-3}, 3×10^{-5}, and 2×10^{-6}, for all parameter combinations. In all panels parallel and perpendicular velocity components are expressed in units of the thermal speed of the core ($\alpha_\perp = \alpha_\parallel$).

have shown that the field-aligned WHFI has larger growth rates (Gary et al. 1975) than the oblique case. We use the core-strahlo distribution given by Equation (1) as the background distribution f_e for the electrons. As already mentioned, to perform the integrals involved, we assume that the electron skewness is small, i.e., $\delta_s^3 \ll 1$. This approximation allows us to obtain an expression for the dispersion tensor elements $D_i = D_i(\omega, k, pp)$ up to second order in δ_s for the parallel-propagating modes. These elements depend on the wavenumber k, the wave frequency ω, and the macroscopic parameters of the initial distribution functions (number density, temperature, etc.), here denoted as a whole by pp. Furthermore, as the distribution is a superposition of Maxwellian and skew-Kappa, the elements of D_i depend on the Fried and Conte plasma dispersion function $Z(\xi)$ (Fried & Conte 1961) and also on the modified dispersion function $Z_\kappa(\xi)$ (Hellberg & Mace 2002; Viñas et al. 2015; Moya et al. 2021). Full expressions of each element of the dispersion tensor can be found in Appendix B. Here we describe the results obtained in the analysis of the excitation of the parallel-propagating whistler mode associated with the heat flux instability.

To obtain the linear properties of the WHFI, we solve the complex dispersion relation using our own developed dispersion solver. We use the core-strahlo distribution (1) to model the eVDF, and the proton population is described by an isotropic Maxwellian such that quasi-neutrality and zero-current conditions

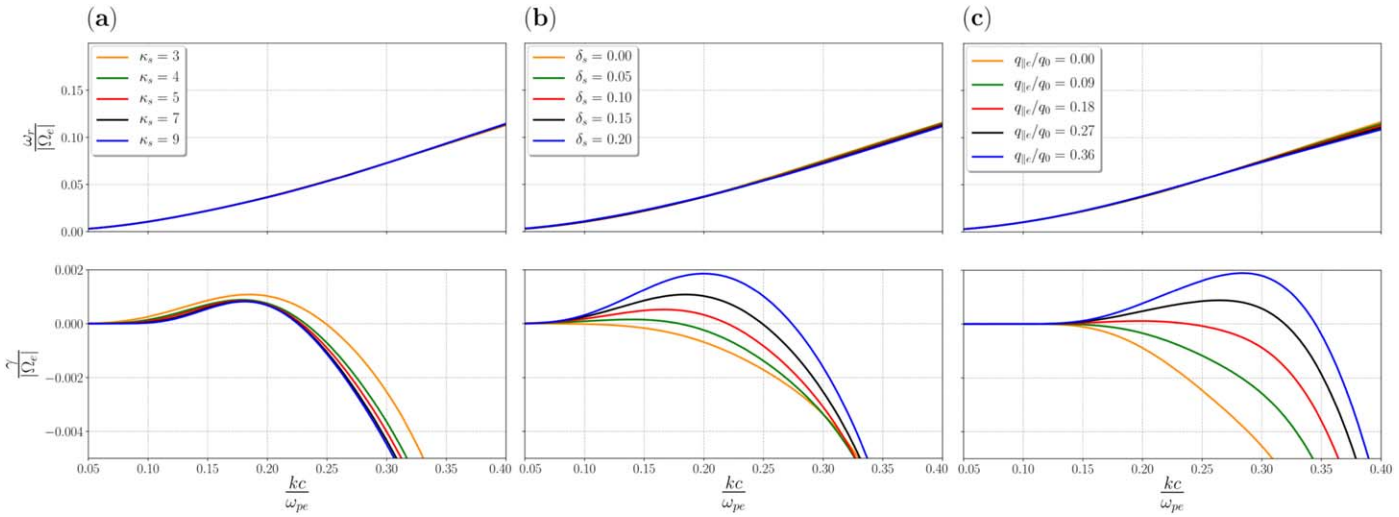

Figure 4. Real (top) and imaginary (bottom) parts of the dispersion relation for the whistler mode for (a) $\delta_s = 0.15$ and different κ_s values, (b) $\kappa_s = 3.0$ and different δ_s values, and (c) a core-halo model composed of two drifting Maxwellians with the same heat flux moment as shown in panel (b) for each value of δ_s. In all cases we set the anisotropy for the electron core and strahlo (or core and halo) equal to 1, $n_s/n_e = 0.1$, $\beta_{\|s} = 1.0$, and $T_{\|s}/T_{\|c} = T_h/T_c = 7.0$.

are both fulfilled. Throughout this analysis we denote proton and electron parameters with subindexes p and e, respectively. We fix the proton distribution so that $\beta_{\|p} = 0.1$ and $T_{\perp p}/T_{\|p} = 1.0$, where $\beta_{\|j} = 8\pi n_j k_B T_{\|j}/B_0^2$ corresponds to the parallel plasma beta of the population j. Also, k_B is the Boltzmann constant, and n_j is the species number density. For the electrons, we fix the anisotropy of both components (core and strahlo) equal to 1, i.e., $T_{\perp s}/T_{\|s} = T_{\perp c}/T_{\|c} = 1.0$, so that there is no free energy associated with the anisotropy of the eVDF. We also fix the density of the strahlo population to 10%. With this selection of parameters for protons and electrons, the only relevant nonthermal features of the electron distribution throughout this work are enhanced tails represented by the κ_s parameter and the skewness represented by δ_s. We perform the stability analysis of the WHFI for different values of δ_s, κ_s, $\beta_{\|s}$, and $T_{\|s}/T_{\|c}$, to study how the dispersion relation depends on these parameters. Further, as in the solar wind at 1 au from the Sun, in all our calculations we have fixed the ratio between the electron plasma frequency (ω_{pe}) and gyrofrequency (Ω_e) to $\omega_{pe}/|\Omega_e| = 200$.

Figures 4(a) and (b) show the real (top) and imaginary (bottom) parts of the frequency of the whistler mode for different values of κ_s and δ_s, respectively, fixing $\beta_{\|s} = 1.0$ and strahlo-to-core parallel temperature ratio $T_{\|s}/T_{\|c} = 7.0$ (Maksimovic et al. 2005; Pierrard et al. 2016; Lazar et al. 2020). Frequency and wavenumber are expressed in units of the electron gyrofrequency, Ω_e, and electron inertial length, $c/|\omega_{pe}|$, where c is the speed of light. Figure 4(a) shows the dispersion relation of the whistler mode considering different values of κ_s and fixed skewness parameter ($\delta_s = 0.15$). We can see that the real frequency remains essentially the same when we modify κ_s and the growth rates slightly decrease as κ_s increases. The case $\kappa_s = 3.0$ corresponds to the most unstable case. As shown in Figures 3(c) and (d), κ_s does not control the symmetry of the distribution. Therefore, it is also reasonable for the wave stability to slightly depend on κ_s. Regarding the dependence on the skewness parameter, Figure 4(b) shows the dispersion relation of the whistler mode for different values of δ_s, fixing $\kappa_s = 3.0$. We can see that, in the wavenumber range shown, the real part of the frequency does not change considerably when we increase δ_s. The imaginary part, however, depends more strongly on this parameter, and the wave becomes more unstable as δ_s increases. Also, the wavenumber range in which the mode is unstable widens, and the k value corresponding to the maximum growth rate also increases with increasing δ_s. Further, note that this relation is nonlinear. For example, when $\delta_s = 0.1$ the maximum growth rate reaches a value $\gamma_{max} \sim 5 \times 10^{-4}\,|\Omega_e|$, whereas for $\delta_s = 0.2$ the maximum growth rate is $\gamma_{max} \sim 2 \times 10^{-3}\,|\Omega_e|$. This behavior is expected because δ_s represents a measurement of the system's free energy associated with the distribution skewness. As δ_s increases, the more skewed the distribution becomes, as we saw in Figures 3(a) and (b). Therefore, the relation between the maximum growth rate of the WHFI and the skewness parameter is also expected to be nonlinear.

Additionally, Figure 4(c) shows similar plots but considering two drifting isotropic Maxwellians given by Equation (2), so that electrons follow a current-free core-halo model as in Gary et al. (1994). Under this model, the normalized electron $q_{\|e}/q_0$ heat flux along the magnetic field is given by $q_{\|e}/q_0 \simeq (5/3)(n_c n_h/n_e^2)(\Delta U_{ch}/\alpha_c)(T_h/T_c - 1)$, where T_h and T_c are the temperature of the halo and core, respectively, and ΔU_{ch} is the relative drift between core and halo (Gary et al. 1994). As a comparison with the core-strahlo model, we consider core and halo with the same density, temperatures, and plasma beta as core and strahlo. We also select ΔU_{ch} such that for each δ_s value shown in Figure 4(b) both models have the same heat flux moment (we will present more details about the heat flux of the core-strahlo model in Section 3.1). Comparing Figures 4(b) and (c), we can see that the dispersion relations obtained by using the skew-Kappa core-strahlo model or the Maxwellian core-halo model are qualitatively the same. Both models produce the same real part of the dispersion relation and are similarly unstable to the WHFI. Nevertheless, differences do exist. In particular, for the same level of heat flux moment the maximum growth of the Maxwellian core-halo model is shifted to larger wavenumber compared to the core-strahlo model. The slight differences between both results are due to the fact that they are based on different mathematical functions, which have different shapes and velocity gradients (i.e., the dispersion relation depends on these gradients) in the valid domain, and perhaps also due to the Taylor expansion to second order on the skewness parameter (not present in a Maxwellian description of the plasma). Furthermore, and to the

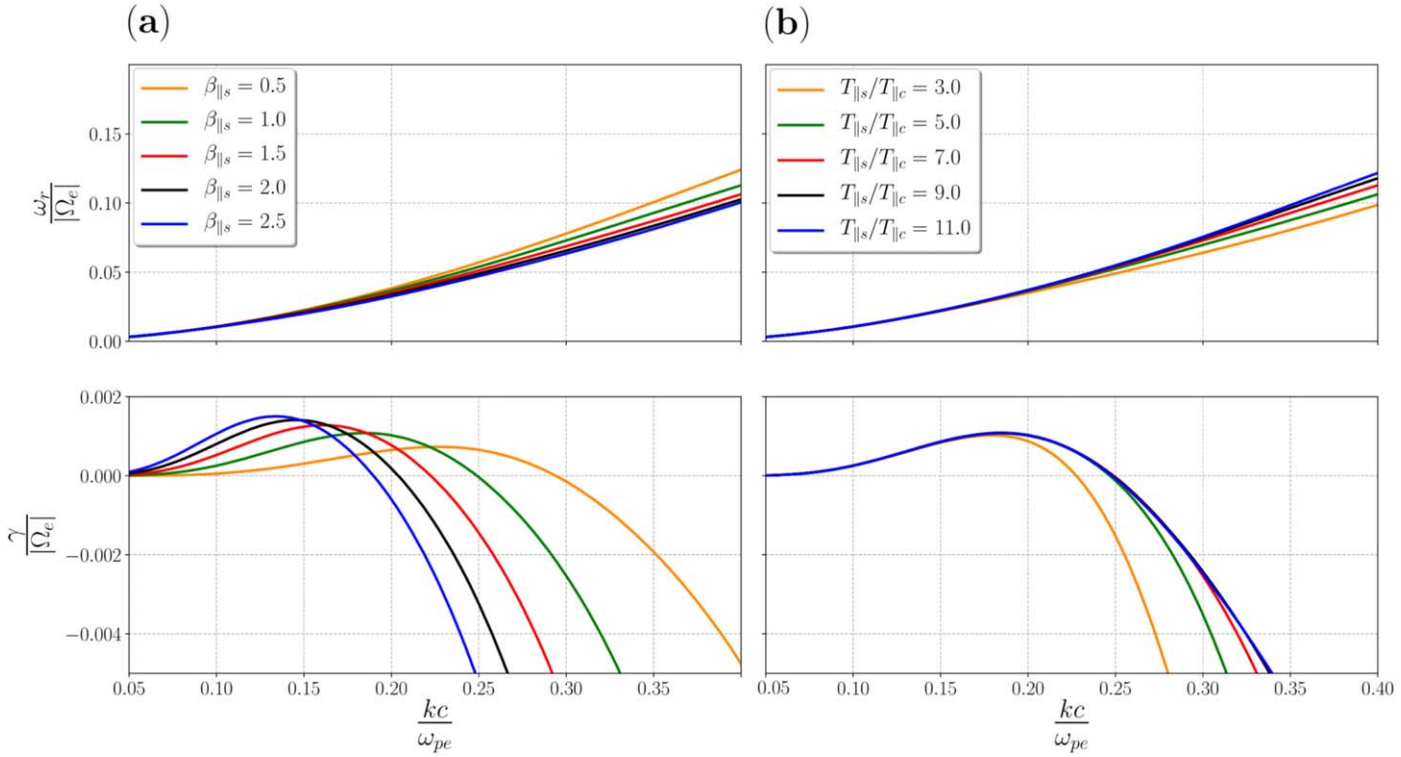

Figure 5. Real (top) and imaginary (bottom) parts of the dispersion relation for the whistler mode for (a) $T_{\|s}/T_{\|c} = 7.0$ and different $\beta_{\|s}$ values and (b) $\beta_{\|s} = 1.0$ and different $T_{\|s}/T_{\|c}$ values. In all cases we set the anisotropy for the electron core and strahlo equal to 1, $n_s/n_e = 0.1$, $\kappa_s = 3.0$, and $\delta_s = 0.15$ for the calculations.

best of our knowledge, these slight differences in the dispersion profiles between the two models have been postulated before, e.g., by Abraham-Shrauner & Feldman (1977a, 1977b) (and probably extend back to the early work of Bernsteinmodes; Bernstein 1958) in application to whistler and electromagnetic ion cyclotron waves in the solar wind, which indicated not only that wave dispersion characteristics are dependent on the physical moment parameters (e.g., density, temperature, drifts, heat flux) but also that they also depend on the shape of the distribution. In this case the differences lay on the lack of suprathermal tails in the Maxwellian model or the fact that in the core-strahlo model the source of asymmetry is strongly dominated by the skewness parameter, not present in the Maxwellian core-halo approach. However, as shown by Figures 4(b) and (c), these are minor differences. Both models can adequately describe the WHFI in the small skewness regime. We can definitely conclude that the results of the core-strahlo model are a very good approximation to the heat flux instability problem, since they reproduce similar behavior to what was previously reported, reinforcing the validity of the model (see Section 2.1).

Finally, Figure 5 shows again the normalized real and imaginary frequencies (top and bottom, respectively) of the whistler mode for different values of $\beta_{\|s}$ and $T_{\|s}/T_{\|c}$, for fixed $\delta_s = 0.15$ and $\kappa_s = 3.0$. Figure 5(a) shows the dispersion relation of the whistler mode for different values of $\beta_{\|s}$ and fixed $T_{\|s}/T_{\|c} = 7.0$. From the figure we can see that in this case the real part of the frequency slightly decreases as $\beta_{\|e}$ increases. On the other hand, as expected, the imaginary frequency depends more strongly on the plasma beta. All cases shown in the plot have a range in which the growth rate is positive, so the plasma is unstable to the whistler mode under these conditions, and it is clear that for higher $\beta_{\|s}$ values the maximum growth rate is also higher. Here, however, the wavenumber at which the growth rate crosses the axis from positive to negative values shifts to the left as $\beta_{\|s}$ increases, i.e., the range in which the growth rate becomes positive narrows. Therefore, as a general rule, we can say that for low values of k the growth rates increase with $\beta_{\|s}$ and the amplitude of the waves grows faster. At the same time, as $\beta_{\|s}$ increases, the wave becomes stable for lower values of the wavenumber. This behavior is also expected since for higher β values the plasma is less magnetized, meaning that the plasma is more susceptible to destabilize owing to electromagnetic fluctuations (Viñas et al. 2015; Moya et al. 2021). Further, Figure 5(b) shows the solutions of the dispersion relation for $\beta_{\|s} = 1.0$ and different values of the strahlo-to-core ratio $T_{\|s}/T_{\|c}$. From the figure we can see that in this case the real part of the frequency increases with increasing $T_{\|s}/T_{\|c}$. The growth rate also increases with the strahlo-to-core temperature ratio, an expected behavior, as a larger temperature of the only electron component providing the free energy for the instability should also result in a larger growth rate of the waves. However, the maximum value of the growth rate seems to saturate to $\gamma_{\max} \sim 10^{-3}\,|\Omega_e|$ at $kc \sim 0.2\,\omega_{pe}$ for $T_{\|s}/T_{\|c} \gtrsim 5$. This is an interesting result, however, as the main goal of our study is the analysis of the WHFI in the solar wind; from now on we will fix $T_{\|s}/T_{\|c} = 7$ and focus the analysis on the effect of the κ_s and δ_s parameters.

3.1. The Effect of the Heat Flux Moment on the Instability

We are particularly interested in understanding how the WHFI contributes to the electron heat flux regulation through collisionless wave–particle interactions in the solar wind. Thus, we expand our stability analysis and study how the whistler wave changes as we modify the electron field-aligned heat flux moment of the eVDF. The connection between the parallel electron heat flux ($q_{\|e}$) and the parameters describing the

electron distribution function (1) can be seen in Equation (9), namely, up to second order in δ_s, $q_{\parallel e}$ is given by

$$q_{\parallel e} = \frac{m_e\, n_s\, \theta_\parallel^3}{4}\, \delta_s \times \left[\mu_s \Psi_6(\kappa_s) + \Psi_7(\kappa_s) + \frac{1}{4}\frac{\alpha_\parallel^2}{\theta_\parallel^2}(3 + 2\mu_c)\right], \quad (9)$$

where Ψ_6 and Ψ_7 are functions that depend only on κ_s and $\mu_j = T_{\perp j}/T_{\parallel j}$ is the anisotropy of population j (see Appendix A for details). Further, to express the heat flux as a dimensionless quantity, it is customary to normalize $q_{\parallel e}$ to the free-streaming or saturation heat flux $q_0 = (3/2) n_e k_B T_{\parallel c}\, \alpha_\parallel$ (see, e.g., Gary et al. 1994). Taking this into consideration, we can write the normalized heat flux as follows:

$$\frac{q_{\parallel e}}{q_0} = \frac{\delta_s}{3}\frac{n_s}{n_e}\left(\frac{T_{\parallel s}}{T_{\parallel c}}\right)^{\frac{3}{2}} \times \left[\mu_s \Psi_6(\kappa_s) + \Psi_7(\kappa_s) + \frac{1}{4}\frac{T_{\parallel c}}{T_{\parallel s}}(3 + 2\mu_c)\right]. \quad (10)$$

In this expression it is clear that the normalized electron heat flux increases linearly with δ_s. In this case (when all other parameters are fixed), as we increase δ_s, $q_{\parallel e}/q_0$ also increases and the plasma becomes more unstable to the whistler mode, just like we saw in Figure 4(a). In other words, if the heat flux increases linearly with δ_s, a larger value of $q_{\parallel e}/q_0$ corresponds to a more skewed distribution and therefore indicates a larger level of free energy to excite the WHFI. In contrast, functions $\Psi_5(\kappa_s)$ and $\Psi_6(\kappa_s)$ indicate that the heat flux decreases as κ_s increases. In this case, as we increase $q_{\parallel e}/q_0$, the stability of the plasma to the whistler mode remains essentially the same, just like Figure 4(b) suggests, i.e., when the increase in heat flux values is a consequence of changes in κ_s, such an increment is due to the modification of the high-energy tails, which are enhanced when κ_s decreases but do not change the symmetry of the eVDF.

To further analyze the behavior of the heat flux parameter, in Figure 6 we plot the normalized growth rates $\gamma/|\Omega_e|$ of the whistler mode as a function of the normalized wavenumber for different values of the initial normalized electron heat flux $q_{\parallel e}/q_0$. We calculate this parameter using different combinations of κ_s and δ_s and fixing $\beta_{\parallel s} = 1.0$ and $T_{\parallel s}/T_{\parallel c} = 7$. Again, we considered isotropic electron populations ($\mu_c = \mu_s = 1.0$) and a 10% density for the strahlo ($n_s/n_e = 0.1$). Blue lines correspond to $q_e/q_0 = 0.02$, red lines to $q_e/q_0 = 0.03$, and green lines to $q_e/q_0 = 0.04$. The line styles differentiate the combinations of parameters used. We see that for the same value of q_e/q_0 the stability of the whistler mode changes depending on the chosen parameters. In this plot, the combinations with higher δ_s (dashed lines) are always more unstable to this mode: the growth rates are positive in a wider wavenumber range, and the maximum growth rate is higher as well. Another thing that should be noticed is that for higher κ_s values higher δ_s values are needed to achieve the same heat flux value.

Accordingly, for a fixed value of κ_s, the heat flux parameter is a direct measurement of the distribution function's skewness and hence of the plasma stability (see solid lines in Figure 6). In this case, we can safely say that the higher the initial heat flux value, the more unstable the whistler mode will be. In contrast, for a fixed δ_s, we cannot make the same straightforward association between the heat flux and the plasma stability since changing the heat flux value will not necessarily affect the stability of the whistler mode. Things get more interesting when we allow the variation of both parameters in calculating the initial heat flux, because the same value of q_e/q_0 can be achieved using different combinations of κ_s and δ_s. Since only the latter parameter significantly impacts the distribution's skewness, different combinations will have different stability for the whistler mode. In other words, systems whose distributions have different levels of asymmetry and, therefore, different stability to the whistler mode can have the same heat flux value. Hence, the heat flux parameter can no longer be a direct measurement of this nonthermal feature (the asymmetry of the eVDF), which gives the plasma the free energy to radiate electromagnetic waves. In consequence, it is not definitive to assure that higher heat flux values represent more unstable states.

4. WHFI Instability Thresholds

As mentioned, one of the goals of this research is an understanding about under which plasma conditions the WHFI develops, as well as to contrast the theoretical predictions with observational data. To do so, in this section we systematize our analysis on the excitation of the WHFI and calculate the instability thresholds for this wave mode in the $q_{\parallel e}/q_0$ versus $\beta_{\parallel s}$ space. We calculate the normalized maximum growth rate of the WHFI, $\gamma_{\max}/|\Omega_e|$, as a function of the normalized electron heat flux $q_{\parallel e}/q_0$ and the electron beta parameter $\beta_{\parallel s}$. Regarding the macroscopic plasma parameters, for protons we consider the same parameters as mentioned in the previous section. For the electrons, as in the previous section we consider isotropic populations ($T_{\perp s}/T_{\parallel s} = T_{\perp c}/T_{\parallel c} = 1.0$) and a density of 10% for the strahlo population ($n_s/n_e = 0.1$). We also use $\kappa_s = 3.0$ and $T_{\parallel s}/T_{\parallel c} = 7.0$. With this choice of parameters, $q_{\parallel e}/q_0$ is a direct measure of the distribution skewness, as can be seen in Equation (10). Figure 7 shows a contour plot of the maximum growth rate of the WHFI for $0.1 \leqslant \beta_{\parallel s} \leqslant 10$ and $1.8 \times 10^{-3} \leqslant q_{\parallel e}/q_0 \leqslant 0.45$, which, following Equation (10), corresponds roughly to $0.001 \leqslant \delta_e \leqslant 0.25$. From the figure we can see that the general behavior for $\gamma_{\max}$ is to increase to the right and upward in the plot, i.e., as expected, the waves become more unstable as $\beta_{\parallel s}$ and $q_{\parallel e}/q_0$ increase. Therefore, we recover the behaviors seen in Figures 4(a) and (b).

Furthermore, to analyze the effect of κ_s on the instability, we repeat the calculations for three different κ_s values (3.0, 4.0, and 5.0). In all cases, we calculate the maximum growth rate in the same δ_s and $\beta_{\parallel s}$ ranges and use the same proton and electron parameters stated before. However, as the core represents most of the solar wind electrons, to facilitate comparisons with observational data, we express the growth rates as a function of parallel beta of the core. Moreover, for each value of κ_s we fit these stability thresholds using a generalized Lorentzian function given by

$$\frac{q_{\parallel e}}{q_0} = A + \frac{B}{(\beta_{\parallel c} + \beta_0)^\alpha}, \quad (11)$$

and we adjust Equation (11) to the contour $\gamma_{\max}/|\Omega_e| = 10^{-3.0}$. In Table 1 we show the parameters A, B, β_0, and α of the best fit for every value of κ_s. We show these parameters to allow easier

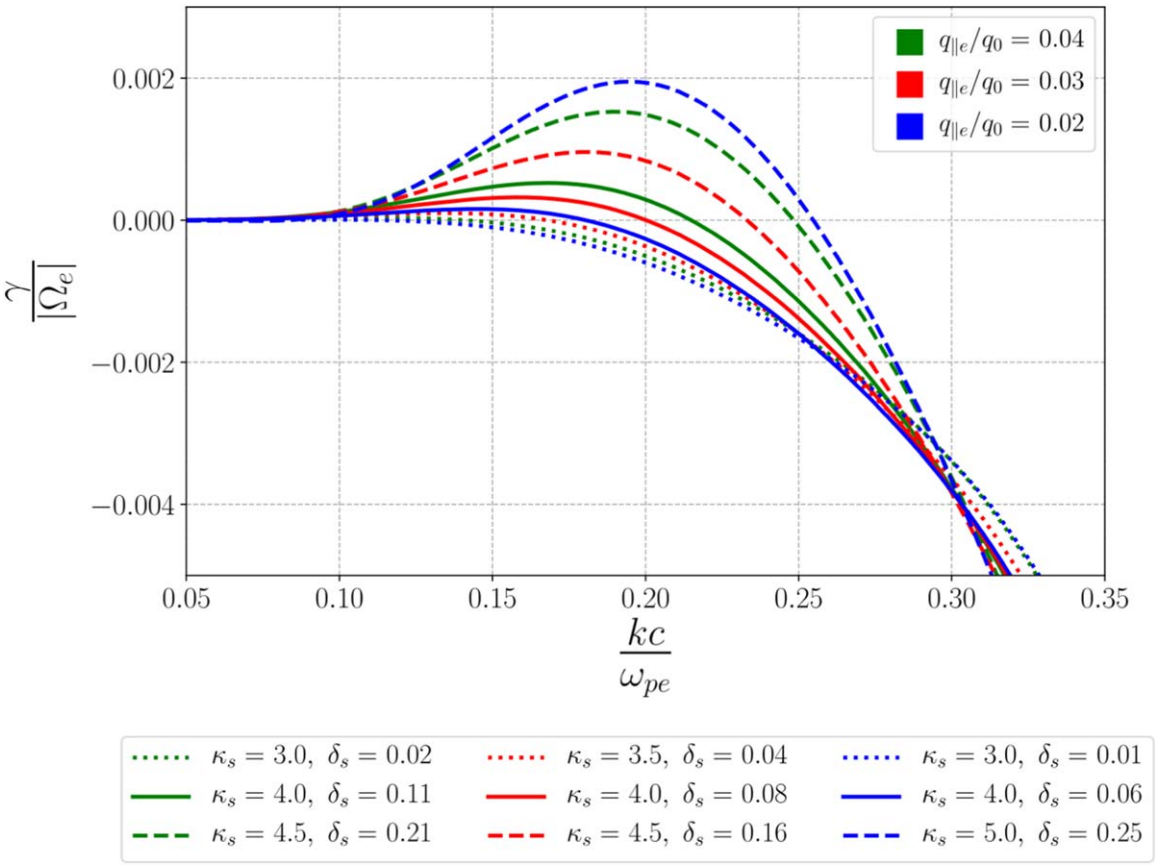

Figure 6. Growth rates of the whistler mode for $\beta_{\|s} = 1.0$, $\mu_c = \mu_s = 1.0$, $T_{\|s}/T_{\|c} = 7$, $n_s/n_e = 0.1$, and different normalized heat flux values: $q_{\|e}/q_0 = 0.02$ (blue lines), $q_{\|e}/q_0 = 0.03$ (red lines), and $q_{\|e}/q_0 = 0.04$ (green lines). As the same heat flux can be achieved by multiple combinations of electron parameters, for each value of the heat flux the growth rates have been derived using three distinct (κ_s, δ_s) combinations, differentiated by line style (solid, dashed, and dotted lines).

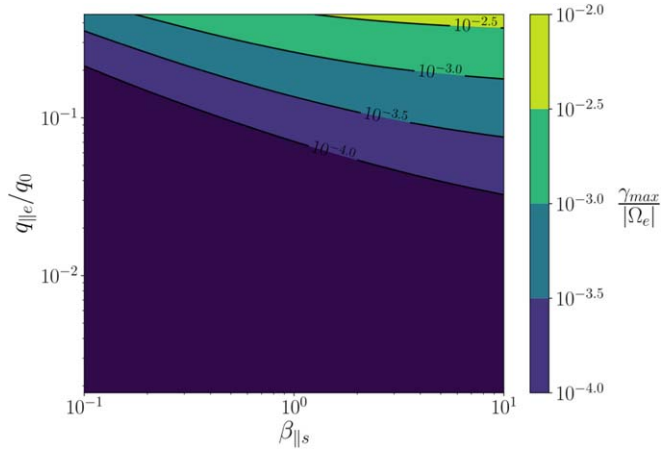

Figure 7. Maximum growth rate of the WHFI, normalized to the electron gyrofrequency $\gamma_{\max}/|\Omega_e|$ for $\kappa_s = 3.0$, as a function of the strahlo parallel beta $\beta_{\|s}$ and normalized parallel electron heat flux $q_{\|e}$. The contours shown correspond to the thresholds $\gamma_{\max}/|\Omega_e| = 10^{-2.5}, 10^{-3.0}, 10^{-3.5}, 10^{-4.0}$, and all calculations were performed using $\mu_c = \mu_s = 1.0$, $T_{\|s}/T_{\|c} = 7$, and $n_s/n_e = 0.1$.

comparison between these instability thresholds and solar wind observations. Figure 8 shows all of these fits and how the threshold changes for different κ_s values. Blue, red, and green lines correspond to $\kappa_s = 3.0$, 4.0, and 5.0, respectively. From the figure we can see that for a fixed $q_{\|e}$ the plasma predominantly becomes more unstable as κ_e increases. This behavior is consistent

Table 1
Best-fit Parameters for the $\gamma_{\max}/|\Omega_e| = 10^{-3}$ Threshold of the Whistler Heat Flux Instability

	A	B	β_0	α
$\kappa_e = 3.0$	0.150	0.132	0.049	0.636
$\kappa_e = 4.0$	0.032	0.033	0.042	0.683
$\kappa_e = 5.0$	0.007	0.008	0.039	0.697

Note. The curve fitting for this threshold was performed using the function shown in Equation (11) for different κ_s and fixing $\mu_c = \mu_s = 1.0$, $T_{\|s}/T_{\|c} = 7$, and $n_s/n_e = 0.1$.

with the results shown in Section 3.1, because as κ_s increases, higher δ_s values are needed in order to achieve the same heat flux. In other words, as κ_s increases, more skewed distributions are needed to achieve a given $q_{\|e}/q_0$, so more free energy is available in the system to excite waves, which translate into higher growth rates, as we saw in Figure 4(a). Therefore, all these results seem to strengthen our previous conclusion that it is not possible to make a direct relation between the heat flux moment and the stability of the plasma to the WHFI.

5. Summary and Conclusions

Using linear kinetic theory, we have performed a stability analysis of the parallel-propagating whistler mode associated with the heat flux instability in a noncollisional and magnetized

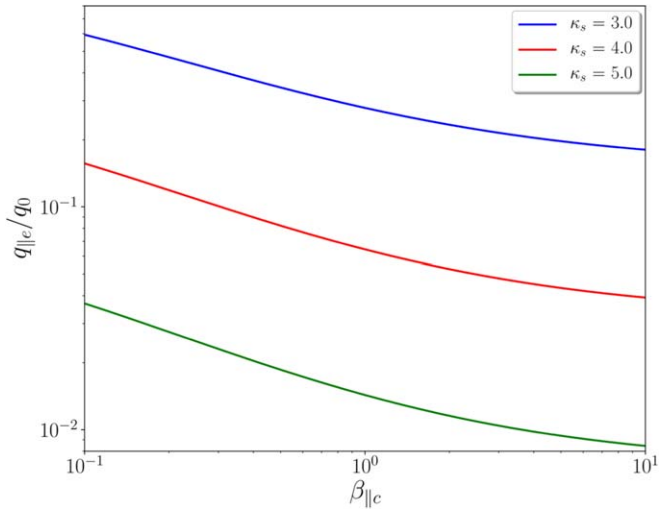

Figure 8. Fits for the instability thresholds of the WHFI for $\kappa_s = 3$ (blue line), $\kappa_s = 4$ (red line), and $\kappa_s = 5$ (green line). The thresholds shown here correspond to maximum growth rates $\gamma_{\max}/|\Omega_e| = 10^{-3}$. All calculations were performed using $\mu_c = \mu_s = 1.0$, $T_{\parallel s}/T_{\parallel c} = 7$, and $n_s/n_e = 0.1$.

plasma, considering parameters typical of the solar wind. Using the Vlasov–Maxwell system, we calculated the dispersion tensor for parallel-propagating waves and solved, numerically, the dispersion relation for the whistler mode. To do so, we introduced the *core-strahlo* model, to describe solar wind electrons as a superposition of a quasi-thermal bi-Maxwellian core and the *strahlo*, which represent halo and strahl populations, using a single skew-Kappa distribution function. Observations inspired the usage of this function, as it reproduces adequately the high-energy tails (measured by the κ_s parameter) of the halo and the skewness (measured by the skewness parameter δ_s) introduced by the strahl as seen in the in situ measurements of the solar wind eVDF.

Notwithstanding the above, since the skew-Kappa distribution always has a singularity for any finite value of δ_s, the use of the core-strahlo model is restricted to electron distributions exhibiting small skewness (i.e., $\delta_s^3 \ll 1$), such that the singularity is far away from the main core of the distribution in units of the thermal speed. As shown in Section 2.1, in those cases all relevant features of the VDF can be represented through a Taylor series approximation around $\delta_s = 0$, and the singularity can be evaded. Using this model, in the case of small skewness we have studied the effects and sensitivity of different plasma parameters over the excitation of the WHFI, such as κ_s, $\beta_{\parallel s}$, $T_{\parallel s}/T_{\parallel c}$, and the skewness parameter δ_s. We focused our attention on the effect that the macroscopic parameter $q_{\parallel e}$ has on the mode's stability since this is the parameter that has been customarily used as a measurement of the eVDF skewness, which is the nonthermal feature in the system that provides the energy for the excitation of the WHFI. We also characterized the β-dependent marginal stability thresholds as a function of the parallel electron heat flux parameter, and we present threshold conditions for the instability that can be modeled to compare with observational data.

Our results showed that when $\delta_s > 0$ the plasma is unstable to the parallel-propagating WHFI and that the growth rates increase with increasing δ_s, which is the parameter that controls the skewness of the eVDF. In addition, we also showed that κ_s (the parameter controlling the extent of the high-energy power-law tails of the distribution) has a weak effect on the stability of this mode: as we increase its value, the mode becomes slightly more stable. Furthermore, we presented the analytical expression for the normalized electron heat flux. For the isotropic case ($\mu_e = 1$) we showed that it is not possible to definitely predict how the growth rates will modify as we increase the electron heat flux. This behavior results from the fact that a given $q_{\parallel e}/q_0$ value can be achieved by multiple (κ_s, δ_s) combinations. Therefore, the stability of the whistler mode depends greatly on how $q_{\parallel e}/q_0$ is calculated in terms of δ_s and κ_s. Finally, to allow comparison with observations, we presented the best-fit parameters, where a generalized Lorentzian has been used for the curve fitting of these stability thresholds. Considering that in this model only δ_s controls the distribution skewness and that high δ_s values (rather than high q_e/q_0 values) are consistent with more unstable states, our results suggest that studies regarding the excitation of the WHFI should be mostly focused on the distribution skewness (a purely kinetic property of the VDF) instead of the heat flux moment, which is a fluid quantity of the plasma. Under this context, we expect these results to provide a new framework to study the role of the WHFI on the depletion of the field-aligned electron heat flux below the values predicted by the collisional transport model and clearly observed by Bale et al. (2013). Moreover, we also expect our results to motivate the search for new methods to measure or estimate the skewness or asymmetry of the eVDF from observations, rather than the field-aligned heat flux moment.

That being said, it is worth mentioning that a skew distribution can also be unstable to other microinstabilities. In particular, as recently shown by López et al. (2020a, 2020b), electron distribution functions composed by a core and a beam can be unstable to several instabilities. However, the electrostatic instability is the fastest-growing mode only when the relative drift between core and beam is larger than the thermal speed. Furthermore, even when the electrostatic mode is faster than the electromagnetic instability, its saturation level is also faster but lower than the electromagnetic. Therefore, the electromagnetic mode dominates in the nonlinear regime. In the case of our study, by construction the relative drift between core and strahlo is smaller than the thermal speed. Thus, the electrostatic instability may be present, but the instability triggered by the skewness (the heat flux instability) should dominate. Due to this reason, and also because of the particular interest of the community on the possible role of the WHFI on the regulation of solar wind heat flux through wave–particle interactions, we have decided to focus only on the WHFI. Nevertheless, we acknowledge the possible existence of more instabilities due to the different nonthermal properties of the electron distribution (temperature anisotropy, asymmetry, relative drifts, power-law tails, etc.). We believe that it is important to address the coexistence and interplay of these instabilities, and we expect to perform such analysis in a subsequent study.

As previously mentioned, to our knowledge the skew-Kappa function has never been used in a space plasma context. In the original derivation of this type of distribution in the context of turbulent flows, Beck (2000) showed that the inverse of the asymmetry term $1/\delta_s$, is proportional to the square root of the Reynolds number ($\mathrm{Re}^{1/2}$). Also, a quick calculation shows that Re is inversely proportional to the Knudsen number Kn ($\mathrm{Re} \propto \mathrm{Kn}^{-1}$). As Kn is directly related to the heat flux transport

in a collisional plasma (Spitzer & Härm 1953; Bale et al. 2013), this relation between δ_s and Kn suggests that δ_s can potentially be related to parameters relevant to the turbulence phenomenon and plasma collisionality, making a possible connection between the kinetic properties of the plasma (the skewness) and a fluid description of the media (the Knudsen number). Therefore, the core-strahlo model based on the skew-Kappa distribution can be more than an ad hoc representation of solar wind electrons. Even though the detailed explanation of such a relation is beyond the scope of this work, we strongly believe that theoretical studies that can link these parameters in plasma systems should be investigated further. For example, as mentioned in Bale et al. (2013), the transition between the collisional Spitzer–Härm heat flux transport and the collisionless regimes occurs at Kn $\sim$0.3. Therefore, using Equation (10), in terms of δ_s our model predicts that such a transition should occur at $\delta_s \sim 0.2$ for $\kappa_s = 3$, $n_s/n_e = 0.1$, $T_{\parallel s}/T_{\parallel c} = 7.0$, and $\mu_c = \mu_s = 1$.

In summary, through the introduction of the core-strahlo model we have showed that plasma states with the same initial heat flux could have different stability from the WHFI. In other words, systems with high $q_{\parallel e}/q_0$ values can be stable enough so that the WHFI cannot modify the electron heat flux values effectively through wave–particle interactions. Thus, the heat flux by itself does not seem to be the best indicator of the WHFI. The precise source of the field-aligned heat flux instability is the skewness of the distribution, and in the case of the skew-Kappa, such a nonthermal feature is clearly represented by the skewness parameter δ_s. The use of the skew-Kappa eVDF allows the distribution skewness to be controlled through just one parameter and considerably reduces the space of free parameters to analyze. Furthermore, the core-strahlo model represents an alternative approach to the usual functions used to phenomenologically model the eVDF in terms of a superposition of three electron subpopulations: core, halo, and strahl. This new model to describe the eVDF greatly simplifies the study of WHFI and the role this instability plays in the electron thermal energy transport in the solar wind. Finally, the use of this distribution has a potential theoretical justification that should be explored, as δ_s could be related to the turbulence phenomenon in plasma systems and also be relevant for the understanding of the relation between the strahl and the formation of the halo during the expansion of the solar wind from the outer solar corona to the heliosphere. Under this context, since the general case with arbitrary skewness remains to be solved, our results suggest that future research about the collisionless heat flux transport in the solar wind should be centered on the distribution skewness (encapsulated here by the δ_s parameter), rather than just the heat flux parameter. We expect this theoretical analysis inspired by observations to be relevant and provide valuable insights in the solar wind electron heat flux regulation debate. Hopefully, the results shown here will be validated with experimental data in light of the new Parker Solar Probe and Solar Orbiter missions.

We acknowledge the support of ANID, Chile, through the Doctoral National Scholarship No. 21181965 (B.Z.-Q.) and FONDECyT grant No. 1191351 (P.S.M.). A.F.-V. would like to thank the Catholic University of America/IACS and NASA-GSFC for their support during the development of this work.

Appendix A
Macroscopic Parameters

In this appendix we show expressions for the relevant macroscopic parameters of the skew-Kappa distribution function f_s shown in Equation (3). In order to perform the integrals in velocity space involved in these expressions, we assume a small skewness (i.e., $\delta_s^3 \ll 1$) and compute these macroscopic parameters using a Taylor expansion of Equation (3) up to second order in δ_s. As usual, in the following equations the subscripts $\parallel$ and $\perp$ are with respect to the background magnetic field:

1. Taylor expansion of f_s,

$$f_s(v_\perp, v_\parallel) = n_s A_s [F_0(v_\perp, v_\parallel) - \delta_s F_1(v_\perp, v_\parallel) + \tfrac{\delta_s^2}{2} F_2(v_\perp, v_\parallel) + \mathcal{O}(\delta_s^3)], \tag{A1}$$

where

$$F_0(v_\perp, v_\parallel) = \left[1 + \frac{1}{\kappa_s - \frac{3}{2}}\left(\frac{v_\perp^2}{\theta_\perp^2} + \frac{v_\parallel^2}{\theta_\parallel^2}\right)\right]^{-(\kappa_s+1)},$$

$$F_1(v_\perp, v_\parallel) = \left[\frac{\kappa_s + 1}{\kappa_s - \frac{3}{2}}\right]\left[\frac{v_\parallel}{\theta_\parallel} - \frac{v_\parallel^3}{3\theta_\parallel^3}\right] \times \left[1 + \frac{1}{\kappa_s - \frac{3}{2}}\left(\frac{v_\perp^2}{\theta_\perp^2} + \frac{v_\parallel^2}{\theta_\parallel^2}\right)\right]^{-(\kappa_s+2)},$$

and

$$F_2(v_\perp, v_\parallel) = \frac{\delta_s^2}{2}\left[\frac{\kappa_s + 1}{\kappa_s - \frac{3}{2}}\right]\left[\frac{\kappa_s + 2}{\kappa_s - \frac{3}{2}}\right] \times \left[\frac{v_\parallel}{\theta_\parallel} - \frac{v_\parallel^3}{3\theta_\parallel^3}\right]^2 \left[1 + \frac{1}{\kappa_s - \frac{3}{2}}\left(\frac{v_\perp^2}{\theta_\perp^2} + \frac{v_\parallel^2}{\theta_\parallel^2}\right)\right]^{-(\kappa_s+3)}.$$

2. Number density,

$$n_s = \int f_s \, d^3v = n_s A_s \times \frac{[(\kappa_s - 3/2)\pi]^{\frac{3}{2}}\theta_\perp^2 \theta_\parallel \Gamma(\kappa_s - 1/2)}{\Gamma(\kappa_s + 1)}\left[1 + \frac{\delta_s^2}{4}\Psi_1(\kappa_s)\right], \tag{A2}$$

where we have defined

$$\Psi_1(\kappa) = \left(\frac{2\kappa - 1}{2\kappa - 3}\right) - \frac{7}{12}. \tag{A3}$$

Therefore, under this regime, the normalization constant A_s in terms of the number density is given by

$$A_s = \frac{\Gamma(\kappa_s + 1)}{[(\kappa_s - 3/2)\pi]^{3/2}\theta_\perp^2 \theta_\parallel \Gamma(\kappa_s - 1/2)}\left[1 - \frac{\delta_s^2}{4}\Psi_1(\kappa_s)\right]. \tag{A4}$$

3. Parallel bulk velocity,

$$U_s = \frac{1}{n_s}\int v_\parallel f_s \, d^3v = -\frac{\delta_s}{4}\theta_\parallel. \tag{A5}$$

4. Perpendicular temperature,

$$T_{\perp s} = \frac{m_s}{2n_s k_B}\int v_\perp^2 f_s\ d^3v = \frac{m_s\ \theta_\perp^2}{2k_B}\left[1 + \frac{\delta_s^2}{4}\Psi_2(\kappa_s)\right], \quad \text{(A6)}$$

where

$$\Psi_2(\kappa) = \frac{5}{12}\left(\frac{2\kappa-3}{2\kappa-5}\right) - \left(\frac{2\kappa-1}{2\kappa-3}\right) + \frac{7}{12}. \quad \text{(A7)}$$

5. Parallel temperature,

$$T_{\parallel s} = \frac{m_s}{n_s k_B}\int (v_\parallel - U_s)^2 f_s\ d^3v = \frac{m_s\ \theta_\parallel^2}{2k_B}\left[1 + \frac{\delta_s^2}{4}\Psi_3(\kappa_s)\right], \quad \text{(A8)}$$

where we have defined

$$\Psi_3(\kappa) = \frac{35}{12}\left(\frac{2\kappa-3}{2\kappa-5}\right) - \left(\frac{2\kappa-1}{2\kappa-3}\right) - \frac{23}{12}. \quad \text{(A9)}$$

6. Parallel heat flux,

$$q_{\parallel s} = \frac{1}{2}m_s\int (\vec{v} - \vec{U}_s)^2 (v_\parallel - U_s) f_s\ d^3v = \frac{m_s\ n_s\ \theta_\parallel^3}{8}\ \delta_s[\mu_s\Psi_4(\kappa_s) + \Psi_5(\kappa_s)],$$

where

$$\Psi_4(\kappa) = \left(\frac{2\kappa-3}{2\kappa-5}\right) - 1 \quad \text{(A10)}$$

and

$$\Psi_5(\kappa) = \frac{5}{2}\left(\frac{2\kappa-3}{2\kappa-5}\right) - \frac{3}{2}. \quad \text{(A11)}$$

Thus, the parallel heat flux for the total electron distribution (1) is given by

$$q_{\parallel e} = \frac{m_e\ n_s\ \theta_\parallel^3}{4}\ \delta_s\left[\mu_s\Psi_6(\kappa_s) + \Psi_7(\kappa_s) + \frac{1}{4}\frac{\alpha_\parallel^2}{\theta_\parallel^2}(3 + 2\mu_c)\right], \quad \text{(A12)}$$

where

$$\Psi_6(\kappa) = \frac{1}{2}\left(\frac{2\kappa-3}{2\kappa-5}\right) - 1 \quad \text{(A13)}$$

and

$$\Psi_7(\kappa) = \frac{5}{4}\left(\frac{2\kappa-3}{2\kappa-5}\right) - \frac{3}{2}. \quad \text{(A14)}$$

Appendix B
Dispersion Tensor

In a noncollisional and uniform plasma, immersed in a background magnetic field $\boldsymbol{B_0} = B_0\hat{z}$, for parallel-propagating waves $\boldsymbol{k} = k\hat{z}$, the dispersion tensor $\mathcal{D}$ can be written in the following form:

$$\mathcal{D}(\omega, k, f_j) = \begin{pmatrix} 1 - \frac{kc^2}{\omega^2} + 4\pi\sum_s \chi_1(f_j) & 4\pi\sum_s \chi_2(f_j) & 0 \\ -4\pi\sum_s \chi_2(f_j) & 1 - \frac{kc^2}{\omega^2} + 4\pi\sum_s \chi_1(f_j) & 0 \\ 0 & 0 & 1 + 4\pi\sum_s \chi_3(f_j). \end{pmatrix} \quad \text{(B1)}$$

The restriction $|\mathcal{D}(\omega, k, f_j)|$ determines the relation between the wave frequency $\omega = \omega_r + i\gamma$ and the wavenumber k for the parallel-propagating modes. In Equation (B1) the dispersion tensor elements are written in terms of the susceptibilities $\chi_i(f_j)$, where the sums are carried out over all species j composing the plasma. The functional form of $\chi_i(f_j)$ depends on the initial distribution function f_j describing population j. Considering the Taylor approximation of the skew-Kappa function f_s shown in Equation (A1), all resonant integrals, relevant for the construction of the dispersion tensor, are reduced to the same integrals necessary to compute to obtain the dispersion relation in a Kappa-distributed plasma as already studied by Summers & Thorne (1991), Mace & Hellberg (1995), and Hellberg & Mace (2002). Therefore, within the small skewness approximation it is safe to assume that all poles and branch cuts have been included, and the integrals do not present any other contribution. Thus, up to second order in δ_s the susceptibilities χ_i of the strahlo take the following form:

$$\chi_1(f_s) = -\frac{\omega_{ps}^2}{4\pi\omega^2} + \frac{1}{8\pi}\frac{\omega_{ps}^2}{\omega^2}\left(\frac{\theta_\perp}{\theta_\parallel}\right)^2 \times \sum_{n=-1,1}\left(\Lambda_n^0 + \delta_s\Lambda_n^1 + \frac{\delta_s^2}{2}\Lambda_n^2\right), \quad \text{(B2)}$$

$$\chi_2(f_s) = \frac{i}{8\pi}\frac{\omega_{ps}^2}{\omega^2}\left(\frac{\theta_\perp}{\theta_\parallel}\right)^2 \times \sum_{n=-1,1} n\left(\Lambda_n^0 + \delta_s\Lambda_n^1 + \frac{\delta_s^2}{2}\Lambda_n^2\right), \quad \text{(B3)}$$

$$\chi_3(f_s) = \frac{1}{2\pi}\frac{\omega_{ps}^2}{k^2\ \theta_\parallel^2}\left(\frac{2\kappa_s - 1}{2\kappa_s - 3}\right)\left(\Lambda_0 + \delta_s\Lambda_1 + \frac{\delta_s^2}{2}\Lambda_2\right), \quad \text{(B4)}$$

where the elements of the expansion are given by

$$\Lambda_n^0 = 1 + \varphi_{n\kappa}Z_\kappa(\xi_{n\kappa}) \quad \text{(B5)}$$

$$\Lambda_n^1 = \frac{1}{2}\sqrt{\frac{\kappa_s}{\kappa_s - \frac{3}{2}}}(1 - \xi_n^2)Z_\kappa(\xi_{n\kappa}) + \frac{1}{2}\left(\frac{\varphi_n}{3} - \xi_n\right) - \left(\frac{\kappa_s - \frac{1}{2}}{\kappa_s - \frac{3}{2}}\right)\left(1 - \frac{\xi_n^2}{3}\right)\varphi_n[1 + \bar{\xi}_{n\kappa}Z_{\kappa+1}(\bar{\xi}_{n\kappa})] \quad \text{(B6)}$$

$$\Lambda_n^2 = \left(\frac{\kappa_s - \frac{1}{2}}{\kappa_s - \frac{3}{2}}\right)\left(\frac{\kappa_s + \frac{1}{2}}{\kappa_s - \frac{3}{2}}\right)\varphi_n\xi_n\left(1 - \frac{\xi_n^2}{3}\right)^2 \times [1 + \tilde{\xi}_{n\kappa}Z_{\kappa+2}(\tilde{\xi}_{n\kappa})] + \frac{1}{2}\left(\frac{\kappa_s - \frac{1}{2}}{\kappa_s - \frac{3}{2}}\right) + \frac{1}{3}\left(\frac{\kappa_s - \frac{1}{2}}{\kappa_s - \frac{3}{2}}\right)\varphi_n\xi_n\left(\frac{\xi_n^2}{6} - 1\right) - \left(\frac{\kappa_s - \frac{1}{2}}{\kappa_s - \frac{3}{2}}\right)(1 - \xi_n^2)\left(1 - \frac{\xi_n^2}{3}\right)[1 + \bar{\xi}_{n\kappa}Z_{\kappa+1}(\bar{\xi}_{n\kappa})] - \frac{\xi_n}{6}\left(\xi_n - \frac{\varphi_n}{2}\right) + \frac{1}{8} - \frac{\Psi_1(\kappa_s)}{2}[1 + \varphi_{n\kappa}Z_\kappa(\xi_{n\kappa})], \tag{B7}$$

for $n = 1, -1$, and

$$\Lambda_0 = 1 + \bar{\xi}_{0\kappa}Z_{\kappa+1}(\bar{\xi}_{0\kappa}) \tag{B8}$$

$$\Lambda_1 = \frac{1}{2}\sqrt{\frac{\kappa_s + 1}{\kappa_s - \frac{3}{2}}}(1 - \xi_0^2)Z_{\kappa+1}(\bar{\xi}_{0\kappa}) - \frac{\xi_0}{3} - \left(\frac{\kappa_s + \frac{1}{2}}{\kappa_s - \frac{3}{2}}\right)\left(1 - \frac{\xi_0^2}{3}\right)\xi_0[1 + \tilde{\xi}_{0\kappa}Z_{\kappa+2}(\tilde{\xi}_{0\kappa})] \tag{B9}$$

$$\Lambda_2 = \left(\frac{\kappa_s + \frac{3}{2}}{\kappa_s - \frac{3}{2}}\right)\left(\frac{\kappa_s + \frac{1}{2}}{\kappa_s - \frac{3}{2}}\right)\xi_0^2\left(1 - \frac{\xi_0^2}{3}\right)^2 \times [1 + \hat{\xi}_{0\kappa}Z_{\kappa+3}(\hat{\xi}_{0\kappa})] - \frac{1}{24}\left(\frac{\kappa_s - \frac{3}{2}}{\kappa_s - \frac{1}{2}}\right) + \frac{1}{2}\left(\frac{\kappa_s + \frac{1}{2}}{\kappa_s - \frac{3}{2}}\right)\left(1 - \frac{\xi_0^2}{3}\right)^2 - \left(\frac{\kappa_s + \frac{1}{2}}{\kappa_s - \frac{3}{2}}\right)(1 - \xi_0^2)\left(1 - \frac{\xi_0^2}{3}\right) \times [1 + \tilde{\xi}_{0\kappa}Z_{\kappa+2}(\tilde{\xi}_{0\kappa})] + \frac{1}{6}\left(1 - \frac{\xi_0^2}{2}\right) - \frac{\Psi_1(\kappa_s)}{2}[1 + \bar{\xi}_{0\kappa}Z_{\kappa+1}(\bar{\xi}_{0\kappa})]. \tag{B10}$$

Finally, for completion, for the core population described by a bi-Maxwellian distribution (2), the susceptibilities χ_i are given by

$$\chi_1(f_c) = -\frac{\omega_{pc}^2}{4\pi\omega^2} + \frac{1}{8\pi}\frac{\omega_{pc}^2}{\omega^2}\left(\frac{\alpha_\perp}{\alpha_\parallel}\right)^2 \times \sum_{n=-1,1}[1 + \phi_n Z(\zeta_n)], \tag{B11}$$

$$\chi_2(f_c) = \frac{i}{8\pi}\frac{\omega_{pc}^2}{\omega^2}\left(\frac{\alpha_\perp}{\alpha_\parallel}\right)^2 \sum_{n=-1,1} n[1 + \phi_n Z(\zeta_n)], \tag{B12}$$

and

$$\chi_3(f_c) = \frac{1}{2\pi}\frac{\omega_{pc}^2}{k^2\ \alpha_\parallel^2}[1 + \zeta_0 Z(\zeta_0)]. \tag{B13}$$

In all of the above expressions $\omega_{pj}^2 = 4\pi n_j q_j^2/m_j$ is the square of the plasma frequency of population j, and $Z(\zeta)$ is the plasma dispersion function, given by

$$Z(\zeta) = \frac{1}{\sqrt{\pi}}\int_{-\infty}^{\infty}\frac{e^{-t^2}}{t - \zeta}\,dt. \tag{B14}$$

In addition, Z_κ is the modified plasma dispersion function (Hellberg & Mace 2002; Viñas et al. 2015, 2017; Moya et al. 2021)

$$Z_\kappa(\xi) = \frac{\Gamma(\kappa)}{\sqrt{\pi\kappa}\ \Gamma(\kappa - 1/2)}\int_{-\infty}^{\infty}\frac{\left(1 + \frac{t^2}{\kappa^2}\right)^{-\kappa}}{t - \xi}\,dt, \tag{B15}$$

which, for any real value of κ such that $\kappa > 1/2$, can be expressed in terms of the Gauss hypergeometric function ${}_2F_1$:

$$Z_\kappa(\xi) = i\frac{\kappa - 1/2}{\kappa^{3/2}}\ {}_2F_1\left[1, 2\kappa; , \kappa + 1; \frac{1}{2}\left(1 - \frac{\xi}{i\kappa^{1/2}}\right)\right]. \tag{B16}$$

Finally, for $n = -1,\ 0,\ 1$ we have defined the following parameters:

$$\xi_n = \frac{\omega - n\Omega_s}{k\theta_\parallel}, \quad \varphi_n = \xi_n + \frac{n\Omega_s u_\parallel}{k\theta_\perp^2}, \quad \zeta_n = \frac{\omega - n\Omega_c - kU_c}{k\alpha_\parallel}, \quad \phi_n = \zeta_n + \frac{n\Omega_c\alpha_\parallel}{k\alpha_\perp^2},$$

$$\xi_{n\kappa} = \xi_n\sqrt{\frac{\kappa}{\kappa - 3/2}}, \quad \bar{\xi}_{n\kappa} = \xi_n\sqrt{\frac{\kappa + 1}{\kappa - 3/2}}, \quad \tilde{\xi}_{n\kappa} = \xi_n\sqrt{\frac{\kappa + 2}{\kappa - 3/2}}, \quad \hat{\xi}_{n\kappa} = \xi_n\sqrt{\frac{\kappa + 3}{\kappa - 3/2}}, \quad \varphi_{n\kappa} = \varphi_n\sqrt{\frac{\kappa}{\kappa - 3/2}},$$

where $\Omega_j = q_j B_0/m_j c$ is the gyrofrequency.

ORCID iDs

Bea Zenteno-Quinteros https://orcid.org/0000-0003-2430-6058
Adolfo F. Viñas https://orcid.org/0000-0001-5912-5703
Pablo S. Moya https://orcid.org/0000-0002-9161-0888

References

Abraham-Shrauner, B., & Feldman, W. C. 1977a, JGR, 82, 1889
Abraham-Shrauner, B., & Feldman, W. C. 1977b, JPlPh, 17, 123
Bale, S., Pulupa, M., Salem, C., Chen, C., & Quataert, E. 2013, ApJL, 769, L22
Beck, C. 2000, PhyA, 277, 115
Bender, C. M., & Orszag, S. A. 1999, Advanced Mathematical Methods for Scientists and Engineers I (New York: Springer)
Bernstein, I. B. 1958, PhRv, 109, 10
Cuperman, S., Harten, A., & Dryer, M. 1972, ApJ, 177, 555
Feldman, W., Asbridge, J., Bame, S., Montgomery, M., & Gary, S. 1975, JGR, 80, 4181
Forslund, D. 1970, JGR, 75, 17

Fried, B. D., & Conte, S. D. 1961, The Plasma Dispersion Function (San Diego, California: Academic)
Gary, S. P., & Feldman, W. 1977, JGR, 82, 1087
Gary, S. P., Feldman, W., Forslund, D., & Montgomery, M. 1975, JGR, 80, 4197
Gary, S. P., & Li, H. 2000, ApJ, 529, 1131
Gary, S. P., Scime, E. E., Phillips, J. L., & Feldman, W. C. 1994, JGRA, 99, 23391
Hellberg, M. A., & Mace, R. L. 2002, PhPl, 9, 1495
Hollweg, J. V. 1974, JGR, 79, 3845
Hollweg, J. V., & Jokipii, J. 1972, JGR, 77, 3311
Horaites, K., Astfalk, P., Boldyrev, S., & Jenko, F. 2018a, MNRAS, 480, 1499
Horaites, K., Boldyrev, S., & Medvedev, M. V. 2018b, MNRAS, 484, 2474
Horaites, K., Boldyrev, S. W., Lynn, B. I., Viñas, A. F., & Merka, J. 2017, MNRAS, 474, 115
Krall, N. A., & Trivelpiece, A. W. 1973, AmJPh, 41, 1380
Kuzichev, I. V., Vasko, I. Y., Soto-Chavez, A. R., et al. 2019, ApJ, 882, 81
Lacombe, C., Alexandrova, O., Matteini, L., et al. 2014, ApJ, 796, 5
Landi, S., Matteini, L., & Pantellini, F. 2012, ApJ, 760, 143
Lazar, M., Fichtner, H., & Yoon, P. 2016, A&A, 589, A39
Lazar, M., Pierrard, V., Poedts, S., & Fichtner, H. 2020, A&A, 642, A130
Lazar, M., Shaaban, S., Poedts, S., & Štverák, Š. 2017, MNRAS, 464, 564
Lazar, M., Yoon, P., López, R., & Moya, P. 2018, JGRA, 123, 6
López, R., Shaaban, S., Lazar, M., et al. 2019, ApJL, 882, L8
López, R. A., Lazar, M., Shaaban, S. M., Poedts, S., & Moya, P. S. 2020a, ApJL, 900, L25
López, R. A., Lazar, M., Shaaban, S. M., Poedts, S., & Moya, P. S. 2020b, PPCF, 62, 075006
Mace, R. L., & Hellberg, M. A. 1995, PhPl, 2, 2098
Maksimovic, M., Zouganelis, I., Chaufray, J.-Y., et al. 2005, JGRA, 110, A09104
Marsch, E., Ao, X.-Z., & Tu, C.-Y. 2004, JGRA, 109, A04102
Marsch, E., Mühlhäuser, K.-H., Schwenn, R., et al. 1982, JGRA, 87, 52
Moya, P. S., Lazar, M., & Poedts, S. 2021, PPCF, 63, 025011
Nieves-Chinchilla, T., & Viñas, A. F. 2008, JGRA, 113, A02105
Olbert, S. 1968, in Summary of Experimental Results from M.I.T. Detector on IMP-1, ed. R. Carovillano, J. McClay, & H. Radoski (Netherlands: Springer), 641
Perkins, F. 1973, ApJ, 179, 637
Pierrard, V., Lazar, M., Poedts, S., et al. 2016, SoPh, 291, 2165
Pierrard, V., Maksimovic, M., & Lemaire, J. 2001, Ap&SS, 277, 195
Pilipp, W., Miggenrieder, H., Mühlhäuser, K.-H., et al. 1987, JGRA, 92, 1103
Rizzo, S., & Rapisarda, A. 2004, in Experimental Chaos: 8th Experimental Chaos Conf., AIP Conf. Proc. 742, ed. S. Boccaletti et al. (Melville, NY: AIP), 176
Saeed, S., Sarfraz, M., Yoon, P., Lazar, M., & Qureshi, M. 2016, MNRAS, 465, 1672
Salem, C., Hubert, D., Lacombe, C., et al. 2003, ApJ, 585, 1147
Sarfraz, M., Saeed, S., Yoon, P., Abbas, G., & Shah, H. 2016, JGRA, 121, 9356
Scime, E. E., Bame, S. J., Feldman, W. C., et al. 1994, JGRA, 99, 23401
Scime, E. E., Littleton, J., Gary, S. P., Skoug, R., & Lin, N. 2001, GeoRL, 28, 2169
Scudder, J. D. 1996, JGRA, 101, 11039
Scudder, J. D., & Olbert, S. 1979, JGRA, 84, 6603
Shaaban, S., Lazar, M., & Poedts, S. 2018a, MNRAS, 480, 310
Shaaban, S., Lazar, M., Yoon, P., & Poedts, S. 2018b, PhPl, 25, 082105
Shaaban, S., Lazar, M., Yoon, P., & Poedts, S. 2019a, ApJ, 871, 237
Shaaban, S., Lazar, M., Yoon, P., Poedts, S., & López, R. 2019b, MNRAS, 486, 4498
Spitzer, L., Jr., & Härm, R. 1953, PhRv, 89, 977
Stix, T. H. 1962, The Theory of Plasma Waves (New York: McGraw-Hill)
Štverák, Š., Maksimovic, M., Trávníček, P. M., et al. 2009, JGRA, 114, A05104
Summers, D., & Thorne, R. M. 1991, PhFlB, 3, 1835
Vasko, I., Krasnoselskikh, V., Tong, Y., et al. 2019, ApJL, 871, L29
Vasyliunas, V. M. 1968, JGR, 73, 2839
Viñas, A., Gaelzer, R., Moya, P., Mace, R., & Araneda, J. 2017, Kappa Distributions (Amsterdam: Elsevier), 329
Viñas, A. F., Moya, P. S., Navarro, R. E., et al. 2015, JGR, 120, 3307
Vocks, C., Salem, C., Lin, R., & Mann, G. 2005, ApJ, 627, 540
Xiao, F., Zhou, Q., Zheng, H., & Wang, S. 2006, JGRA, 111, A08208